Large-Eddy Simulations of Shock/Boundary Layer Interaction in Transient Nozzle Flows

By A. Chaudhuri, A. Hadjadj, T. Gatski† AND R. Friedrich‡
CORIA - INSA & University of Rouen, 76801 St Etienne du Rouvray, France

Large-eddy simulations are carried out to investigate the propagation of shock waves with flow separation and shock/boundary layer interactions associated with shock induced transient flows through a planar nozzle. A high-order WENO scheme based 3D numerical flow solver equipped with an immersed boundary method is used for this purpose. The theoretical shock jump relation, associated with a shock Mach number M_s : 1.86, is utilized to initiate the propagation of the shock wave through the nozzle section within a shock-tube arrangement similar to a laboratory shock-tube experimental setup. Interactions of transverse waves with the developed boundary layer trigger shock induced flow separation inside the nozzle. Improper initialization of the flow-field may lead to erroneous predictions of the flow characteristics, particularly the location of the separation point and the unsteady shock/boundary layer interaction. A comparative study is presented to show the effect of different flow initializations namely, i) without flow fluctuation, ii) with white random noise and iii) with homogeneous isotropic turbulence superimposed on the flow-field. Results are in good agreement with the experimentally measured speeds of the primary shock wave and the following secondary shock wave. Substantial improvement in the prediction of the early-stage Mach reflection, complex shock/boundary layer interaction is observed with superimposed turbulent fluctuations as an initial flow-field.

1. Introduction

Optimization of the nozzle contour to obtain maximum thrust under the limitations of an engine envelope is one of the most important design factors for an effective rocket engine. The classical design approach is based on ideal contours (designed by the method of characteristics, delivering a uniform flow at the nozzle exit), but being significantly truncated to limit the overall thrust chamber length [1]. The demand of higher performance of rocket launchers is inherently associated with the requirement of increasing expansion ratios. However, the presence of flow separation and coupled complex shock structures inside the nozzle cause significant mechanical and thermal loads at higher expansion ratio. Flow separation is typically undesirable since it incurs high energy losses and lateral forces on the structure of the nozzle. The knowledge of the transient process in a supersonic nozzle is important to predict the unsteady behavior of these loads during the startup and shutdown phases. It is considered that for the parabolic and compressed-truncated perfect (CTP) nozzles, the transition of the flow

† Institut Pprime (CNRS) & University of Poitiers, 86036 Poitiers cedex, France
‡ Lehrstuhl für Aerodynamik und Strömungsmechanik, Technische Universität München, Boltzmannstr. 15, 85748 Garching b. München

structure, from free-shock separation (FSS) to restricted-shock separation (RSS) and vice-versa, create the sudden change of the pressure distribution along the nozzle wall, resulting in the generation of strong side-loads. Especially for RSS, the excessive heat load associated with the re-attached supersonic flow at the nozzle wall and the side-load characters have to be mastered by the thermo-mechanical design. Fundamentally, the complex flow features consist of phenomena like shock propagation, shock reflection, shock boundary layer interaction, shock mixing/shear layer interactions. Experimental and numerical studies of shock structures in the plume pattern are presented by many researchers. A comprehensive review of the nozzle flow separation is presented by Hadjadj and Onofri [2]. Nevertheless, studies of the analysis of transient shock induced supersonic flow in nozzles are not abundant in the literature. In his experimental study, Amann [3] first reported the influence of different parameters of nozzle shapes on the starting process of a reflection nozzle. Two dimensional numerical simulations related to this work in a shock-tube setup have been presented by few authors [4–8]. All these numerical predictions were typically able to reproduce the principle phenomena of shock propagation, speeds of secondary shock wave/contact discontinuity. However, their main inadequacy lies in the fact to resolve the 3D turbulence and its strong interactions with the complex shock wave structures and the location of the flow separation. The resolution of all these issues and the associated computational costs are still highly challenging areas of scientific research to be explored.

In the present work, large-eddy simulations are carried out to investigate the propagation of shock waves, flow separation and complex shock wave/boundary layer interaction associated with shock induced transient flows through planar nozzles. The computational domain has been chosen similar to the experimental setup of a shock-tube facility of the Ben-Gurion University, Beer-Sheva, Israel. The report is organized as follows: A brief description of the numerical tools is presented in Sec. 2. Section 3 illustrates the formulation of the numerical setup followed by the results and discussion in Sec. 4. Finally, conclusions and future work are presented in Sec. 5.

2. Numerical method

2.1. *Filtered Navier-Stokes equations*

An implication of Kolmogorov's (1941) theory of self-similarity is that the large eddies of the flow are dependent on the geometry while smaller scales are more universal in nature. This feature allows one to explicitly solve for the large eddies in a numerical simulation and implicitly account for the smaller eddies by using a subgrid scale (SGS) model. The triumphant journey of LES started with the pioneering work of Smagorinsky [9], Lilly [10], Deardoff [11], Germano [12] and others. Comprehensive accounts on LES are provided by Sagaut [13] and Pope [14] and reviews at different stages of the development are provided in [15–18].

The definition of any filtered quantity with a filter function G_Δ and associated filter width $\Delta = (\Delta_x \times \Delta_y \times \Delta_z)^{1/3}$ can be given by,

$$\bar{f}(\vec{x},t) = \int_{R^3} f(\vec{y},t) G_\Delta(\vec{x}-\vec{y}) d\vec{y} \tag{2.1}$$

To reduce the SGS terms, the Favre averaged definition is generally used in compressible flow simulations, defined as, $\tilde{f} = \overline{\rho f}/\bar{\rho}$. Applying the above definitions and neglecting the SGS terms having negligible contributions [19], the filtered compressible

Navier-Stokes system of equations can be written as,

$$\frac{\partial \bar{\rho}}{\partial t} + \frac{\partial \bar{\rho}\tilde{u}_i}{\partial x_i} = 0 \tag{2.2}$$

$$\frac{\partial \bar{\rho}\tilde{u}_i}{\partial t} + \frac{\partial \bar{\rho}\tilde{u}_i\tilde{u}_j}{\partial x_j} + \delta_{ij}\frac{\partial \bar{p}}{\partial x_j} = \frac{\partial \breve{\sigma}_{ij}}{\partial x_j} - \frac{\partial \tau_{ij}}{\partial x_j} \tag{2.3}$$

$$\frac{\partial \bar{\rho}\breve{E}}{\partial t} + \frac{\partial (\bar{\rho}\breve{E} + \bar{p})\tilde{u}_j}{\partial x_j} = \frac{\partial (\tilde{u}_i\breve{\sigma}_{ij})}{\partial x_j} - \frac{\partial \breve{q}_j}{\partial x_j} - \frac{\partial q_j^{sgs}}{\partial x_j} - \tilde{u}_i\frac{\partial \tau_{ij}}{\partial x_j} \tag{2.4}$$

where $\breve{\sigma}_{ij}$ is the resolved stress tensor, $\breve{E}$ is the resolved energy. $\tau_{ij} = \bar{\rho}(\widetilde{u_i u_j} - \tilde{u}_i\tilde{u}_j)$ and q_j^{sgs} are the SGS stress and the SGS heat flux respectively, both of which have to be modeled in order to close the system of equations. In the present work, the Wall-Adapting Local Eddy-viscosity (WALE) model is used to close these SGS terms.

2.2. *WALE model*

The Wall-Adapting Local Eddy-viscosity model proposed by Nicoud and Ducros [21] is basically designed to reproduce more accurate scaling for simulations containing wall boundary conditions. It includes the effect of both the strain and the rotation and thereby gives a better prediction in the region where vorticity dominates irrotational strain. The WALE model reproduces a proper near wall scaling so that the eddy viscosity is $\nu_t = \mathcal{O}(y^3)$. It is estimated from the velocity gradient tensor's invariant as follows,

$$\nu_t = C_w^2\Delta^2\frac{(\tilde{s}_{ij}^d\tilde{s}_{ij}^d)^{3/2}}{(\tilde{s}_{ij}\tilde{s}_{ij})^{5/2} + (\tilde{s}_{ij}^d\tilde{s}_{ij}^d)^{5/4}} \tag{2.5}$$

where C_w is a model constant, $\tilde{s}_{ij} = \frac{1}{2}\left(\frac{\partial \tilde{u}_i}{\partial x_j} + \frac{\partial \tilde{u}_j}{\partial x_i}\right)$ and $\widetilde{s}_{ij}^d$ is the traceless symmetric part of the square of the resolved velocity gradient tensor ($\widetilde{g}_{ij} = \partial\widetilde{u}_i/\partial x_j$), namely, $\widetilde{s}_{ij}^d = \frac{1}{2}\left(\widetilde{g}_{ij}^2 + \widetilde{g}_{ji}^2\right) - \frac{1}{3}\delta_{ij}\widetilde{g}_{kk}^2$ with $\widetilde{g}_{ij}^2 = \widetilde{g}_{ik}\widetilde{g}_{kj}$. The model constant $C_w = 0.5$ is recommended to be optimal from priori tests of freely decaying isotropic homogeneous turbulence. It can be emphasized that, the LES model based on $\widetilde{s}_{ij}^d\widetilde{s}_{ij}^d$ detects turbulence structures with either (large) strain rate, rotation rate or both. Moreover, it avoids any dynamic procedure while maintaining the desired near wall scaling. No eddy-viscosity is being produced in case of wall bounded laminar flow (Poiseuille flow). This is distinctively advantageous over the Smagorinsky model (based on $\tilde{s}_{ij}\tilde{s}_{ij}$, but not on rotation rate) which is unable to reproduce the laminar to turbulent flow transition. The WALE model based on the $\tilde{s}_{ij}^d\tilde{s}_{ij}^d$ invariant is known to be capable of handling the transitional pipe flow [21].

The SGS heat flux, q_j^{sgs} is modeled using the eddy-diffusivity hypothesis assuming constant $Pr_t = 0.72$ and is given by,

$$q_j^{sgs} = -\frac{\mu_t c_p}{Pr_t}\frac{\partial \widetilde{T}}{\partial x_j} \tag{2.6}$$

An in-house 3D compressible Navier-Stokes solver equipped with a fifth-order WENO scheme [22], LES models and an immersed boundary method [23–28] is used for the present simulations. The use of low-dissipation, high-order shock-capturing schemes is an essential ingredient for computing complex compressible flows with shock waves. The objective is to avoid excessive numerical damping of the flow features over a wide range of length scales as well as to prevent spurious numerical oscillations near shock

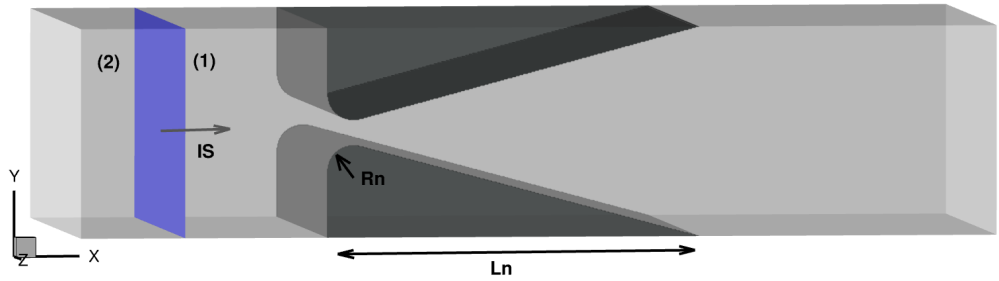

FIGURE 1. Computational setup, IS: Incident Shock wave, Rn = 10 mm, Ln = 142.871 mm, nozzle angle = 15°, throat length, $L_t = 9.5$ mm, $p_1 = 98800$ Pa, $T_1 = 291.5$K, $Re \approx 4.1 \times 10^5$ (based on L_t and properties at the left state).

waves and discontinuities. For instance, the family of WENO schemes is a good choice to achieve this goal. The diffusion terms are determined by means of fourth-order compact central difference formulas. The discretized equations are integrated in time by means of the explicit third-order total variation diminishing Runge-Kutta algorithm (RK3-TVD). The CFL number is set to 0.7 for all simulations. Detailed description of the applied methodology is reported in our previous work [29, 30]. Three-dimensional LESs are carried out for all the cases presented in this paper. The simulations are performed on a SGI Altix ICE 8200EX and an IBM Power6 parallel computer using up to 512 processors consuming about 40960 CPU hours for each test case.

3. Problem formulation

Figure 1 shows the computational setup for all the cases. A shock wave with a prescribed shock Mach number (M_s) is allowed to pass through the nozzle situated at the end test section of the shock-tube arrangement. The Rankine-Hugoniot relations for a moving shock ($M_s = 1.86$) for air is used to set the left state (shocked gas, subscripted as '2') and right state (stagnant gas, subscripted as '1') of the shock wave. In order to compare with experimental findings, the initial position of the shock wave is prescribed at the leading edge of the nozzle. Although the experimental setup is having a cross-section of 80 mm$\times 80$ mm, the computational domain having $(80 \times L_t/2)$ mm^2 cross section is chosen and an immersed boundary technique is utilized to treat the nozzle boundaries within the Cartesian mesh. The top and bottom boundaries are set to no slip conditions while the span-wise direction (z-axis) is considered as homogeneous. Computations are stopped before the shock-wave reaches the left or right boundaries.

Three test cases are formulated as follows, C_1: without initial turbulent velocity fluctuation, C_2 : with turbulent velocity fluctuation taken from a white random noise and C_3 : with turbulent velocity fluctuation according to homogeneous isotropic velocity field. Table 1 summarizes the parameters for three test cases. The centerline density has been recorded to construct the speed of the different dominant shock waves particularly the primary shock (PS) and secondary shock (SS) to compare with the experimental results. Flow field data at numerical probes on the walls of the nozzle are also registered to get the wall properties and their unsteady evolution.

Case	C_1	C_2	C_3
Initial turbulent velocity	Zero	White random noise	Homogeneous isotropic
Domain (mm^3)	$450 \times 80 \times 4.75$	$450 \times 80 \times 4.75$	$350 \times 80 \times 2\pi$
Grid (million points)	172	169	188
$\Delta_x, \Delta_y, \Delta_z$ (μm)	$140, 140, 140$	$120, 50, 170$	$98, 49, 196$
nozzle location (mm)	152	152	94.248

TABLE 1. Parameters for different test cases.

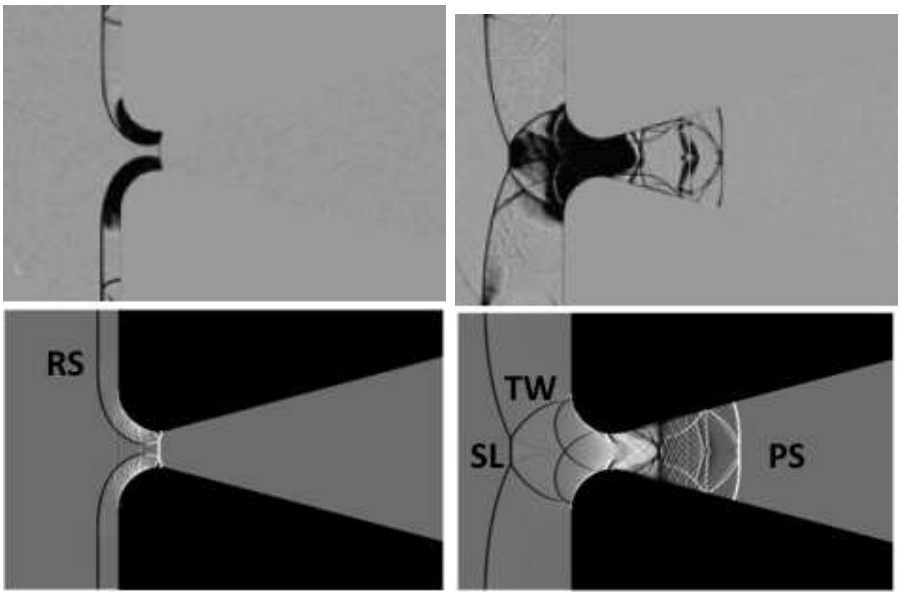

FIGURE 2. Comparison of experimental (top) and numerical (bottom) schlieren at $t \approx 15\mu s$ and $t \approx 65\mu s$, PS: primary shock, RS: reflected shock, TW: transverse wave, SL: slip line.

4. Results and discussion

The flow-field has been averaged in the homogeneous direction to compare the experimental and numerical schlieren pictures. Comparisons of the early stage shock wave structures are shown in Figs. 2 and 3. A part of the incident shock (IS) reflects and returns back upstream of the nozzle section as reflected shock (RS), while the part which entered in the opening variable flow section of the nozzle evolves as primary shock (PS) front, followed by a typical mushroom shaped contact surface (CS) and the boundary layer interaction with transverse reflections gives rise to a secondary shock (SS). It can be seen from these figures that the numerical simulation is able to capture the dominant wave structures of the flow-field.

In order to visualize the propagation of different waves, the X-T diagram has been constructed from the transient density field. Figure 4 clearly shows the evolution of PS, CS and SS. It can be seen that a very good agreement of the shock positions with the experimental results has been found. Deviation of the position of the secondary shock at the later stages, is inevitable due to the inaccuracy of the determination of the exact location of the secondary shock from the first derivative of the density field. From the

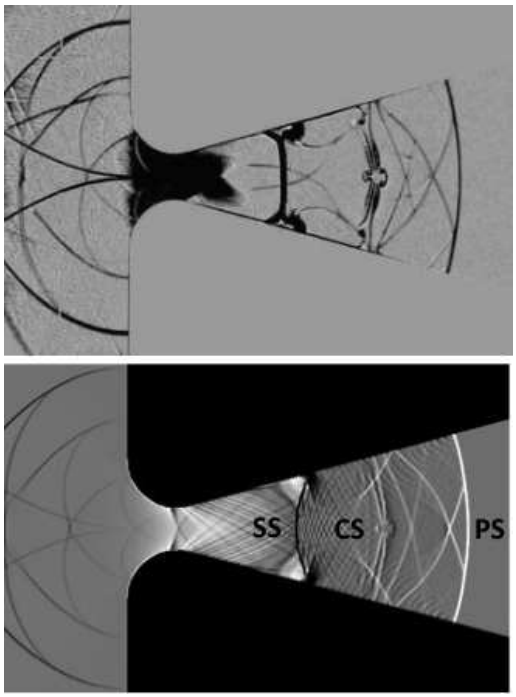

FIGURE 3. Experimental and numerical schlieren at $t \approx 115\mu s$, SS : secondary shock, CS: contact surface, PS: primary shock.

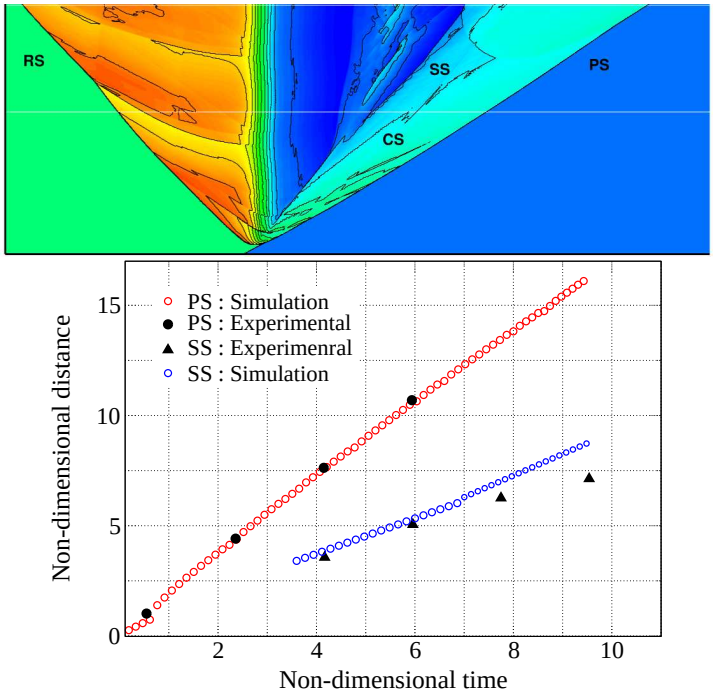

FIGURE 4. X-T diagram : density contour on non-dimensional time (y-axis)and non-dimensional position (centerline) x-axis.

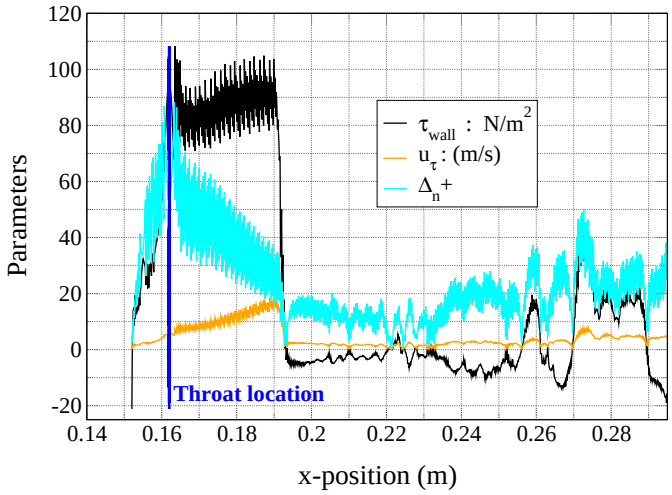

FIGURE 5. Near wall parameters.

registered flow-field data we estimated the near wall properties at $t \approx 613\mu s$ (see Fig. 5). The position of the flow separation can be deduced from the wall shear stress profile. However, it is also clear from this figure that $\Delta_n^+ < 90$ ($\Delta_n^+ = \Delta_n u_\tau / \nu_w$, where u_τ is the friction velocity, ν_w is the kinematic viscosity at the wall and Δ_n is the wall-normal distance of the near wall grid point). However, Δ_n^+ decreases in downstream direction, beginning at the nozzle throat. This brings in the deviations of later stage flow structures when compared with the experimental results. It is evident that the immersed boundary method inherently produces non-smooth boundary (like steps) along the nozzle wall. However, it is also well known that without any artificial turbulence injection, the transition of laminar to turbulent flow will hardly take place numerically, given the present computational setting. The existence of high values of Δ_n^+ clearly indicates the requirement of higher grid resolution for the improvement of the numerical prediction. In order to have an initial fluctuating flow-field, we have formulated case C_2 with an increased grid resolution. A random velocity field with zero mean and unity variance has been superimposed onto the mean flow-field assuming a turbulent intensity of 0.1 as an initial trial.

It is clear from Fig. 6 that the higher grid resolution for C_2 corroborates the fact that the calculated Δ_n^+ is less than 50 which is lower than that of case C_1. It can also be noted that, the flow separation point shifts upstream compared to case C_1. As expected, the speeds of the principal shock waves show identical outcomes for C_1 and C_2. It is worth mentioning that the mean wall pressure and density profiles show symmetrical behavior on top and bottom walls. Nevertheless, inevitable differences in these profiles downstream of the flow separation point are also clearly visible in Fig. 7. The 3D numerical schlieren, Q criterion and vorticity field are shown in Fig. 8 to highlight the 3D flow features and different scales of turbulence. On the other hand, Fig. 9 shows the anisotropic behavior of the Reynolds stresses, indicating that the shear layer region is dominantly turbulent. It can be seen from the velocity vector field (Fig. 10) that, upstream of the separation zone, the flow is virtually laminar and the oblique shocks interact with these laminar boundary layers. This is distinctively different from the experimental observation. It is to be noted that the generation of a fluctuating flow-field with a white random

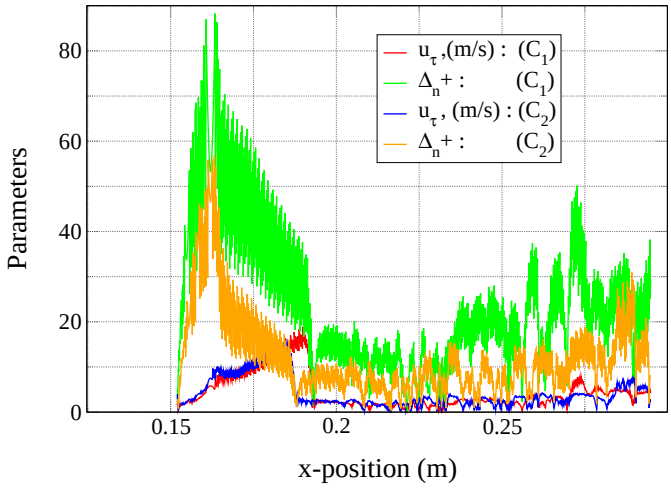

FIGURE 6. Comparison of near wall parameters.

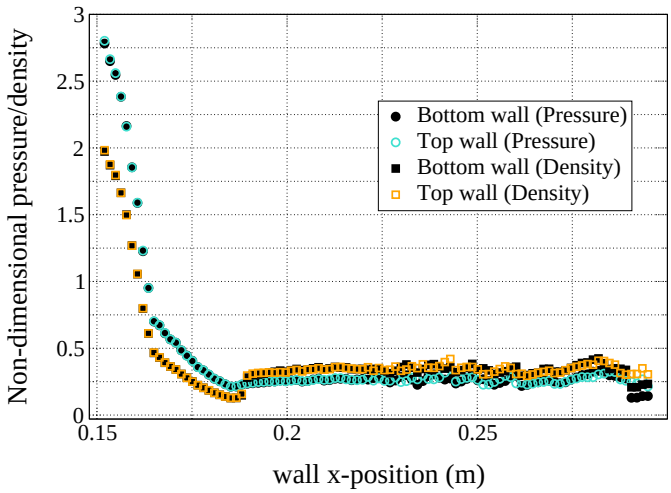

FIGURE 7. Wall distribution for C_2.

L_∞	Re_{ac}	$u_p^\star$	u_p	$k_e^\star$	$l_e^\star$
1 mm	$c_\infty L_\infty/\gamma_\infty$	u_p/c_∞	$0.1U_2$	6	$2\pi/k_e^\star$

TABLE 2. Reference state (∞) is taken as the shocked gas state. c_∞ and γ_∞ are the speed of sound, viscosity at reference state. u_p is the turbulent velocity, $l_e^\star$ is the most energetic length scale and its associated wave number is $k_e^\star$.

noise generator produces a fluctuating flow-field without any correlation of fluctuating components of the velocities.

To improve the initial turbulent flow fluctuations, we formulated the case C_3 with homogeneous isotropic turbulent velocity fluctuations in the shocked gas region. A prescribed

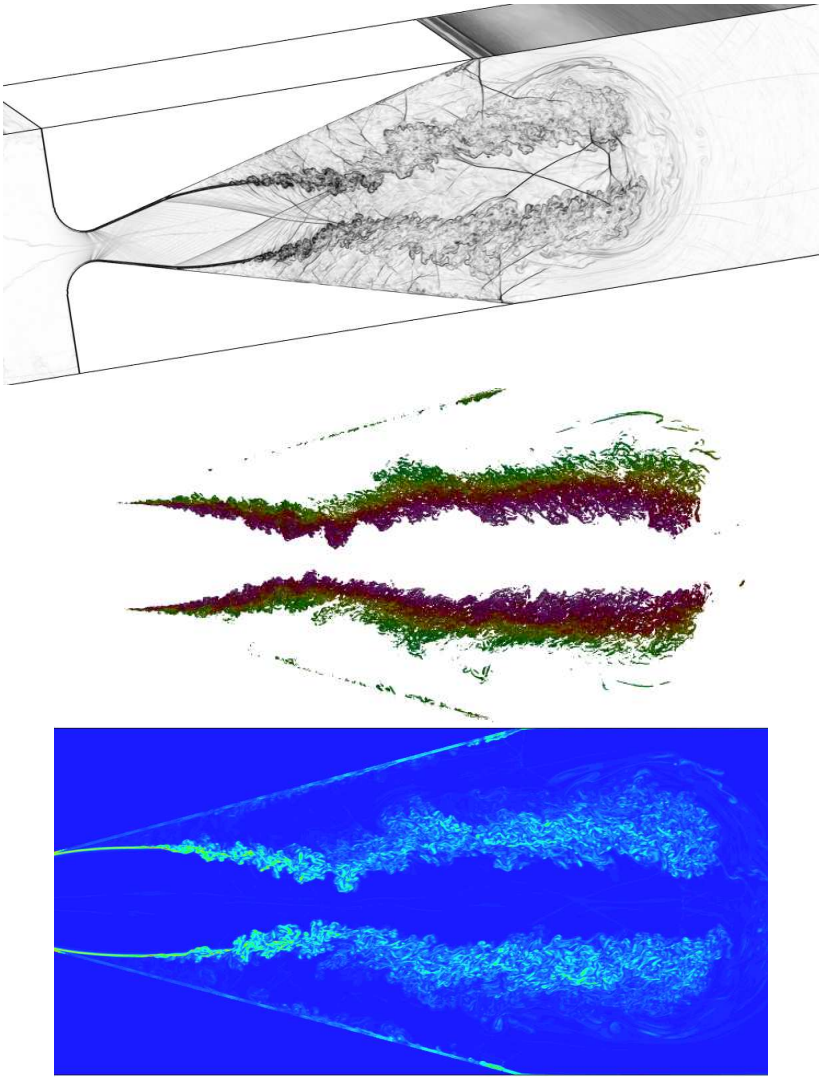

FIGURE 8. Flow visualization for C_2, top: 3D numerical schlieren, bottom: Q iso-surfaces flooded with stream-wise velocity and mid-plane vorticity field.

energy spectrum of Passot-Pouquet, $E(k^\star) = A\left(\frac{k^\star}{k_e^\star}\right)^4 e^{-2\left(\frac{k^\star}{k_e^\star}\right)^2}$ has been assumed to generate the initial velocity field. An open source [31] turbulent flow-field generator code has been used first to get an initial box of turbulent flow-field and this periodic data has been repeatedly assigned to fit in the computational domain of $350 \times 80 \times 2\pi$ mm^3 (see Tab. 1). To generate a $(2\pi)^3$ box of turbulent flow-field, the following inputs are to be assumed, i) Acoustic Reynolds number Re_{ac}, ii) non-dimensional turbulent velocity $u_p^\star$ and iii) most energetic length scale $l_e^\star$.The different parameters used to generate this flow-field are summarized in Tab. 2. Within the timeframe of this project the computations of C_3 is unfinished. However, with the partial results obtained from the simulation, a comparison among the three test cases is shown in Fig. 11. It can be seen from the

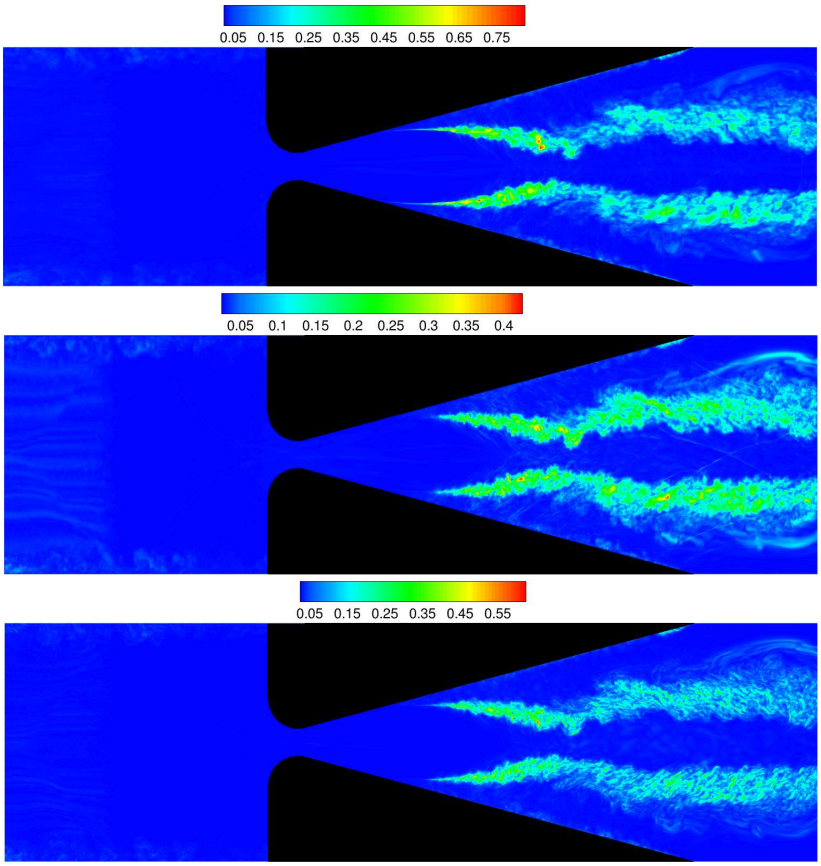

FIGURE 9. Resolved Reynolds stress contour for C_2. From top to bottom: $\sqrt{R_{11}}/U_2$, $\sqrt{R_{22}}/U_2$, $\sqrt{R_{33}}/U_2$, where $R_{ij} = \dfrac{\langle \bar{\rho}\widetilde{u''_i}\widetilde{u''_j}\rangle}{\langle \bar{\rho}\rangle}$. Any average resolved quantity $\langle\widetilde{\phi}\rangle$ is defined as the spatial averaged quantity over homogenous direction and the resolved fluctuating component $\widetilde{\phi''} = \widetilde{\phi} - \langle\widetilde{\phi}\rangle$.

experimental schlieren that the secondary shock is related to a Mach reflection and is attached with the turbulent separated zone. The experimental picture clearly indicates that the boundary layer upstream of the flow separation is turbulent in nature, resulting in a strong shock interaction with the boundary layer. It can also be seen that for C_1, the oblique shock reflections are close to a regular reflection rather than a Mach reflection. The flow features depict the inability to reproduce the turbulent flow-field and coupled interactions. Moreover, the strong expansion fan after the throat region is a clear indication of lacking grid resolution. On the other hand, the existence of a turbulent separation zone and improved shock boundary layer interactions are visible for C_2 and C_3. Again, it can be noted that the deviation from the experimental flow structures are essentially related to the onset of turbulence in the region between throat and flow separation point. The weak Mach reflections predicted by the simulations are related to the nature of the boundary layer upstream of the flow separation. Nevertheless, it is clearly visible that there exists a progressive improvement in the predictions from case C_1 to case C_3.

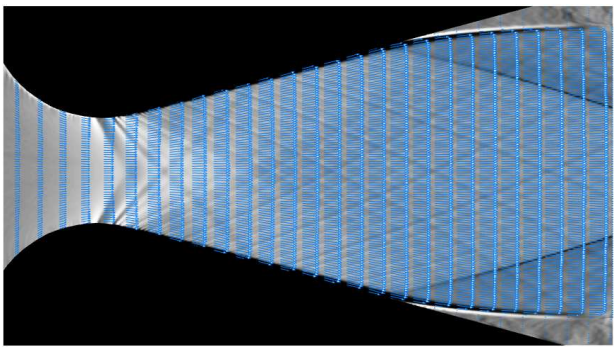

FIGURE 10. Velocity vector plot C_2.

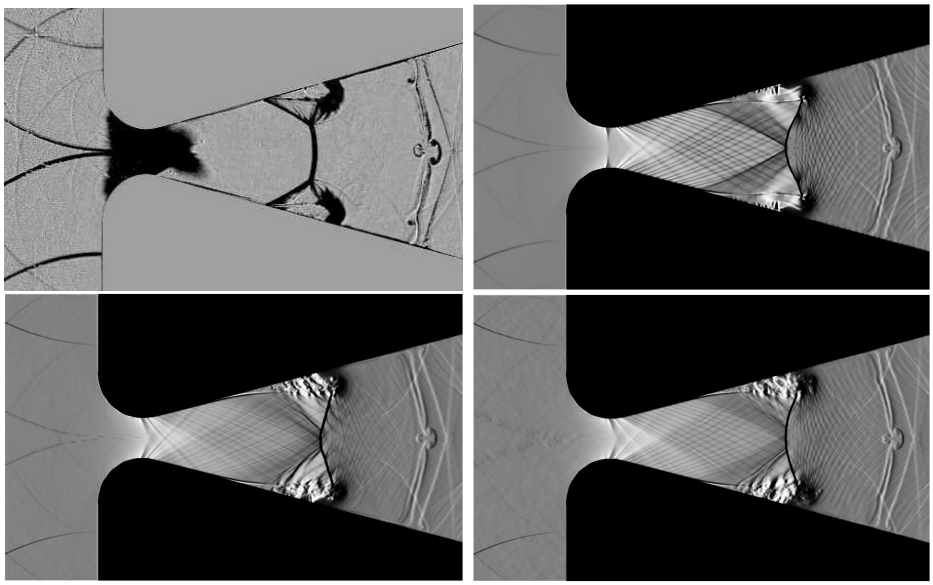

FIGURE 11. Comparison of schlieren pictures at $\approx 165\mu$s top left: experimental, top right: C_1, bottom left: C_2 and bottom right: C_3.

5. Conclusions

In this work, we made an initial attempt to resolve numerically the complex flow features associated with shock induced supersonic flow inside a planar nozzle in a shock-tube arrangement. LESs are carried out with a flow solver equipped with a high-order WENO scheme and an immersed boundary technique. The global flow features of primary, secondary shock waves and contact discontinuity are well captured and in good agreement with the experimental data. Two simulations C_1 and C_2 show quantitative agreement with experiments for the speed of the primary as well as the secondary shocks. Intersection points of the shock-wave on the central line matched qualitatively better with the simulation having initial fluctuations. It is observed that the initial flow-field greatly influences the separation point and the resulting oblique shock structure. The partial results of case C_3 (computations with initial homogeneous isotropic turbulent fluctuating flow-field) show its superiority over the other cases. The lack of information of the initial level of turbulence in the experiments leads to the difficulties involved in the

proper choice of the initial flow-field and the assumption of initial turbulent parameters. Apart from the complete analysis of the results of case C_3, the future work aims at further investigating the influence of the introduction of the fluctuating flow-field in the right state with zero mean velocity. A systematic comparison of the performance of different LES models should also be accomplished.

Acknowledgments

The authors gratefully acknowledge the financial support provided by the German Research Foundation (Deutsche Forschungsgemeinschaft – DFG) in the framework of the Sonderforschungsbereich/Transregio 40 and the IGSSE (International Graduate School of Science and Engineering) at Technische Universität München. We have utilized the computational facilities from GENCI [CCRT/CINES/IDRIS] (grant 2010-0211640) and Leibniz-Rechenzentrum München (LRZ). Authors are also grateful to the group of researchers working with Prof. Gabi Ben-Dor and Dr. Oren Sadot from Ben-Gurion University, Beer-Sheva, Israel, for providing some of their experimental results.

References

[1] HAGEMANN, G. AND FREY, M. (2008). Shock pattern in the plume of rocket nozzles: needs for design consideration. *Shock Waves*, **17**, 387–395.

[2] HADJADJ, A. AND ONOFRI, M. (2009). Nozzle flow separation. *Shock Waves*, **19**, 163–169.

[3] AMANN, H. O. (1969). Experimental study of the starting process in a reflection nozzle. *Shock tube symposium, The physics of fluids supplement I*, I-150-I-153.

[4] TOKARCIK-POLSKY, S. AND CAMBIER, J. L. (1994). Numerical study of transient flow phenomena in shock tunnels. *AIAA J.*, **32**(5), 971–978.

[5] IGRA, O., WANG, L., FALCOVITZ, J. AND AMANN, O. (1998). Simulations of the starting flow in a wedge-like nozzle. *Shock Waves*, **8**, 235–242.

[6] SAITO, T. AND TAKAYAMA, K. (1999). Numerical simulations of nozzle starting process. *Shock Waves*, **9**, 73–79.

[7] MOURONVAL, A. S., HADJADJ, A., KUDRYAVTSEV, A. N. AND VANDROMME, D. (2002). Numerical investigation of transient nozzle flow. *Shock Waves*, **12**, 403–411.

[8] MOURONVAL, A. S. AND HADJADJ, A. (2002). Numerical study of starting process in a supersonic nozzle. *J. Propulsion & Power*, **21**, 2, 374–378.

[9] SMAGORINSKY, J. (1963). General circulation experiments with the primitive equations. I. the basic experiment. *Mon. Weather Rev*, **91**, 99.

[10] LILLY, D. K. (1992). A proposed modification of the Germano subgrid-scale closure method. *Phys. Fluids A*, **4**, 633.

[11] DEARDORFF, J. W. (1974). Three-dimensional numerical study of the height and mean structure of a heated planetary boundary layer. *Boundary Layer Meteorol.*, **7**, 81.

[12] GERMANO, M., PIOMELLI, U., MOIN, P. AND CABOT, W. H. (1991). A dynamic subgrid-scale eddy viscosity model. *Phys. Fluids* , **A 3**, 1760.

[13] SAGAUT, P. (2001). *Large eddy simulation of turbulent flows*. Springer, Berlin.

[14] POPE, S. B. (2000). *Turbulent flows*. Cambridge University Press, Cambridge.

[15] ROGALLO, R. S. AND MOIN, P. (1984). Numerical simulation of turbulent flows. *Ann. Rev. Fluid Mech.*, **16**, 99–137.

[16] GALPERIN, B. AND ORSZAG, S. A. (1993). *Large eddy simulation of complex engineering and geophysical flows*. Cambridge University Press, Cambridge.

[17] LESIEUR, M. AND MÉTAIS, O. (1996). New trends in Large-Eddy Simulations of turbulence. *Ann. Rev. Fluid Mech.*, **28**, 45–82.

[18] MENEVEAU, C. AND KATZ, J. (2000). Scale-invariance and turbulence models for Large-Eddy Simulation. *Ann. Rev. Fluid Mech.*, **32**, 1–32.

[19] DUBOS, S. (2005). *Simulation des grandes échelles d'écoulements turbulents supersoniques*. PhD thesis, LMFN-CORIA, UMR 6614, France.

[20] YOSHIZAWA, A. (1986). Statistical theory for compressible turbulent shear flows, with the application to subgrid modeling. *Phys. Fluids A*, **29**, 2152.

[21] NICOUD, F. AND DUCROS, F. (1999). Subgrid-scale stress modelling based on the square of the velocity gradient tensor. *Flow, Turbulence and Combustion*, **62**, 183–200.

[22] JIANG, G. AND SHU, C. W. (1996). Efficient implementation of weighted ENO schemes. *J. Comp. Phys.*, **126**, 202–228.

[23] PESKIN, C. S. (1972). *Flow patterns around heart valves: a digital computer method for solving the equations of motion*. PhD thesis, Albert Einstein Coll. Med.

[24] MITTAL, R. AND IACCARINO, G. (2005). Immersed boundary methods. *Ann. Rev. Fluid Mech.*, **37**, 239–261.

[25] IACCARINO, G. AND VERZICCO, R. (2003). Immersed boundary technique for turbulent flow simulations. *Appl. Mech. Rev.*, **56**, 331–347.

[26] TSENG, Y. AND FERZIGER, J. H. (2003). A ghost-cell immersed boundary method for flow in complex geometry. *J. Comp. Phys.*, **192**, 593–623.

[27] GAO, T., TSENG, Y. AND LU, X. (2007). An improved hybrid cartesian/immersed boundary method for fluid-solid flows. *Int. J. Numer. Meth. Fluids*, **55**, 1189–1211.

[28] DADONE, A. AND GROSSMAN, B. (2004). Ghost-cell method for inviscid two-dimensional flows on cartesian grids. *AIAA J.*, **42**(12), 2499–2507.

[29] CHAUDHURI, A., HADJADJ, A. AND CHINNAYYA, A. (2011). On the use of immersed boundary methods for shock/obstacle interactions, *J. Comp. Phys.*, **230**, 1731–1748.

[30] CHAUDHURI, A., HADJADJ, A., CHINNAYYA, A. AND PALERM, S. (2011). Numerical study of compressible mixing layers using high-order WENO schemes. *J. Sci. Computing,* **47**(2), 170–197.

[31] THI3DR8 (SOURCE CODE), Generation of incompressible 3D homogeneous isotropic turbulence, available at *http://www.cerfacs.fr*.